Operation of Quantum Plasmonic Metasurfaces Using Electron Transport through Subnanometer Gaps

Publication information:
ACS Photonics, vol.6, no.10, pp.2517-2522, Sept. 2019.
DOI: 10.1021/acsphotonics.9b00889
https://pubs.acs.org/doi/abs/10.1021/acsphotonics.9b00889

Takashi Takeuchi, Masashi Noda, and Kazuhiro Yabana*

Center for Computational Sciences, University of Tsukuba, Tsukuba 305–8577, Japan

KEYWORDS: Quantum plasmonics, metasurface, electron transport, subnanometer gap, time-dependent density functional theory.

ABSTRACT: Herein, we investigate the optical properties of quantum plasmonic metasurfaces composed of metallic nano-objects with subnanometer gaps according to the time-dependent density functional theory, a fully quantum mechanical approach. When the quantum and classical descriptions are compared, the transmission, reflection, and absorption rates of the metasurface exhibit substantial differences at shorter gap distances. The differences are caused by electron transport through the gaps of the nano-objects. The electron transport has profound influences for gap distances of $\lesssim 0.2$ nm; that is, approximately equal to half of the distance found in conventional gap plasmonics in isolated systems, such as metallic nanodimers. Furthermore, it is shown that the electron transport makes the plasmon features of the metasurface washed out and produces broad spectral structures in the optical responses. In particular, the reflection response exhibits rapid attenuation as the gap distance decreases, while the absorption response extends over a wide spectral range.

A plasmonic metasurface within which metallic nano-objects are (a) smaller than the wavelength of the incident light and (b) periodically placed on a plane, has been attracting substantial attention in terms of its highly beneficial optical characteristics for designing various optoelectronic devices.[1–2] Subject to the irradiation of an optical field, the electromagnetic energy of light is confined in the constituent nano-objects as a plasmon—a collective motion of electrons—generating locally enhanced plasmonic fields around the objects. This plasmon property, manifested by its enhanced optical capturing capacity, has opened up many practical applications of the metasurface, such as subdiffraction lensing,[3–4] monochromatic or color holography,[5–8] polarization converters,[9–10] polarization-selective elements,[11–12] and others.[13–14]

In most investigations conducted to date, the optical properties of metasurfaces that are composed of nano-objects whose gap distances are at the wavelength or subwavelength scales have been explored. Recently, experimental studies have reported on metasurfaces with gap distances as small as a subnanometer.[15–16] For example, the optical properties of a plasmonic metasurface with subnanometer gaps made of gold nanospheres coated with tunable alkanethiol ligand shells were reported[16] in which the interparticle distance was controlled from 0.45 to 2.8 nm. It has been found that owing to the significantly intense optical confinement at the gaps, the metasurface yielded a high-refractive index that could not be achieved in naturally occurring transparent materials.

In the last decade, tremendous attention had been paid to subnanometer gap plasmonics in isolated systems with metallic nanodimers constituting a typical paradigm.[17–23] In brief, the research findings were based on interesting observations in which substantial differences existed between descriptions using classical and quantum theories. In the classical description, in which the surface of nanoparticles are modeled as ‘discontinuous’ boundaries, the solutions of Maxwell’s

equations yield an extremely enhanced and confined electromagnetic field at the gap as the nanoparticles come closer to each other. By contrast, in quantum description with 'continuous' boundaries expressed using realistic electron density distributions, the charge transfer processes across the gap that were caused by electron tunneling suppressed the field enhancements, especially at small gap distances ($\lesssim$ 0.4 nm).[17, 19, 21–22, 24] This suppression in the gap plasmonics has been confirmed by experiments.[20, 25–26] It is often crucially important to know when the quantum effect starts to appear; for example, in plasmonic applications that are based on strong optical enhancement and confinement, including in surface-enhanced Raman scattering (SERS) technologies[27–30] and other nanophotonic systems.[31–34]

In view of the broad applicability of metasurfaces, it is particularly concerning how the quantum effects appear in them. However, to the best of our knowledge, there have been no prior experimental or theoretical reports that have discussed the quantum effects. Measurements carried out on the metasurface with a minimum gap distance of 0.45 nm[16] have been reproduced by classical theory. This may be reasonable owing to fact that the effects of electron tunneling on isolated systems with gap distances of $\gtrsim$ 0.4 nm have been small.

In this study, quantum plasmonic metasurfaces composed of metallic nanospheres with subnanometer gaps were theoretically investigated by a fully quantum mechanical method using the time-dependent density functional theory (TDDFT)[35–36] combined with a two-dimensional (2D) course-graining approach.[37] We will show the transmission, reflection, and absorption rates of the metasurface to elucidate the quantum effects in the optical properties. Our results indicate that there are substantial differences between the classical and the quantum descriptions for metasurfaces with gap distances $\lesssim$ 0.2 nm. This gap distance is almost equal to half of the critical threshold distance in isolated systems presented in previous studies.[17, 19–22, 25-26] Our results also

indicate that the quantum effects make the plasmonic features washed out in the frequency domain and produce broad spectral structures in the optical responses at small gap distances. In particular, the reflection shows rapid attenuation as the gap distance decreases, while the absorption extends over a broad frequency range. These findings indicate that they are suitable as optical absorbers.

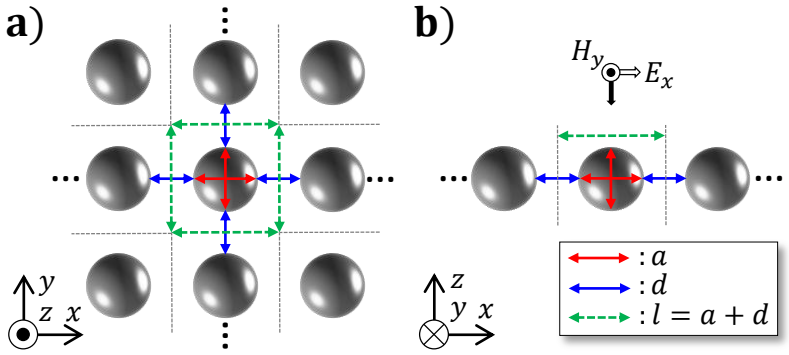

Figure 1. Schematics of the studied metasurface consisting of nanospheres periodically arrayed on the *xy* plane: (a) top and (b) side views. The incident light has E_x and H_y components and propagates toward the negative *z* direction. The symbols *a*, *d*, and *l*, drawn using red, blue, and green arrows, denote the diameters of the spheres, the gap distances, and the lengths of the periods, respectively.

The studied system is displayed in Figure 1a and 1b. In these figures, metallic nanospheres with diameter *a* are periodically arrayed on the *xy* plane with a gap distance *d* and a period length *l*. The incident light is linearly polarized with the E_x and H_y components, and propagates along the negative *z* direction. To take into account quantum mechanical effects with a moderate computational cost, we employed the spherical jellium model (JM) that replaces ionic structures with a positive background charge with a sharp surface. Despite its simplicity, the JM can describe the actual plasmonic behavior of electrons in metallic nanoparticles.[17, 19, 38] In particular, qualitative agreements with measurements have been reported for an isolated metallic nanodimer with a subnanometer gap that accounted for the effects caused by electron tunneling.[20, 25]

In the JM, the Wigner–Seitz radius r_s related to the average charge density, *n*, $n^+ = ((4\pi)r_s^3/3)^{-1}$, specifies the medium. Herein, $r_s = 4.01$ Bohr, which corresponds to the Na metal. Each nanosphere

was set to accommodate 398 electrons that correspond to a closed shell structure. The resultant diameter of the nanosphere a was 3.1 nm. The size is sufficiently large so that the nanoparticle exhibits a typical plasmonic resonance.[21]

To calculate the optical responses of metasurfaces, we employed linear-response TDDFT, which is extensively used for the optical responses of molecules[39] and solids[40] at a first-principles level. We assumed an adiabatic approximation for the exchange-correlation potential and used the local density approximation.[41] Numerical calculations were carried out using SALMON, an open-source code (https://salmon-tddft.jp/) developed in our group.[42] The Supporting Information contains a detailed description of the adopted numerical approach.

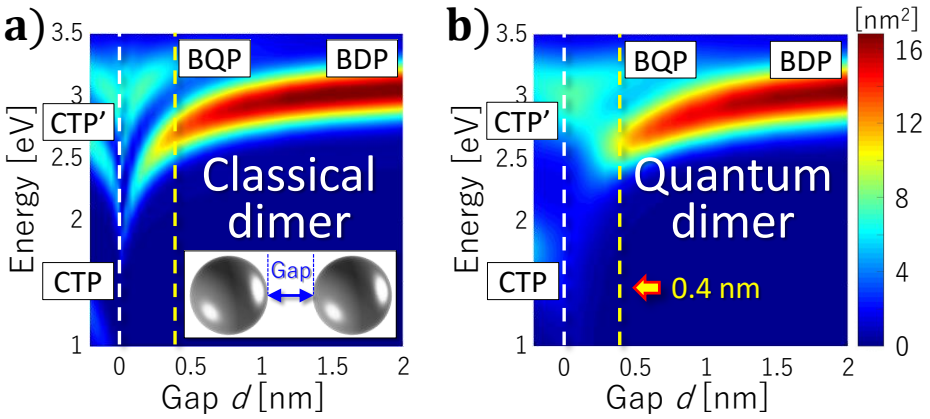

Figure 2. (a) Optical absorption cross-section of a metallic dimer (the inset shows the relevant schematic) calculated based on classical theory, whereby the constituent nanospheres have the same diameters as those in the case of the metasurface, as shown in Figure 1. The horizontal and vertical axes denote the gap distance d and optical frequency, respectively. The white dashed lines indicate the loci at which $d = 0$ nm, while the yellow lines indicates loci at which $d = 0.4$ nm. (b) Results generated by the TDDFT in conjunction with the JM.

First, to facilitate a comparison between the isolated and periodic systems, we briefly describe the optical response of a nanodimer that consists of metallic nanospheres identical to those used in the metasurface calculations. Figure 2a and 2b show the absorption cross-sections of the dimer calculated using the classical theory and the TDDFT, respectively. In the classical theory, the

Drude model was used. Details of the theories are explained in the Supporting Information. In both theories, the absorption properties are dominated by the bonding dipolar plasmon (BDP) mode for gap distances $d \gtrsim 0.4$ nm. The red shift that appears in both theories is caused by the increase in the coupling strength as the two spheres approach each other. However, when $d \lesssim 0.4$ nm, substantial differences can be observed between the two results. In the classical theory, there appears an additional bonding quadrupolar plasmon (BQP) mode at a higher frequency region until $d = 0$ at the contact point of the two spheres. For $d < 0$ nm after the geometrical overlap of the spheres, the charge transfer and its high-order-plasmon (CTP and CTP') modes emerge. By contrast, in the TDDFT, quite different spectral distributions are manifested for $d \lesssim 0.4$ nm. The BDP disappears prior to the direct contact and a hybridized form of the BQP and the CTP becomes visible. This is caused by the charge transfer due to the electron tunneling through the gap region between the nanospheres. These trends had already been established in previous studies.[17, 19–22]

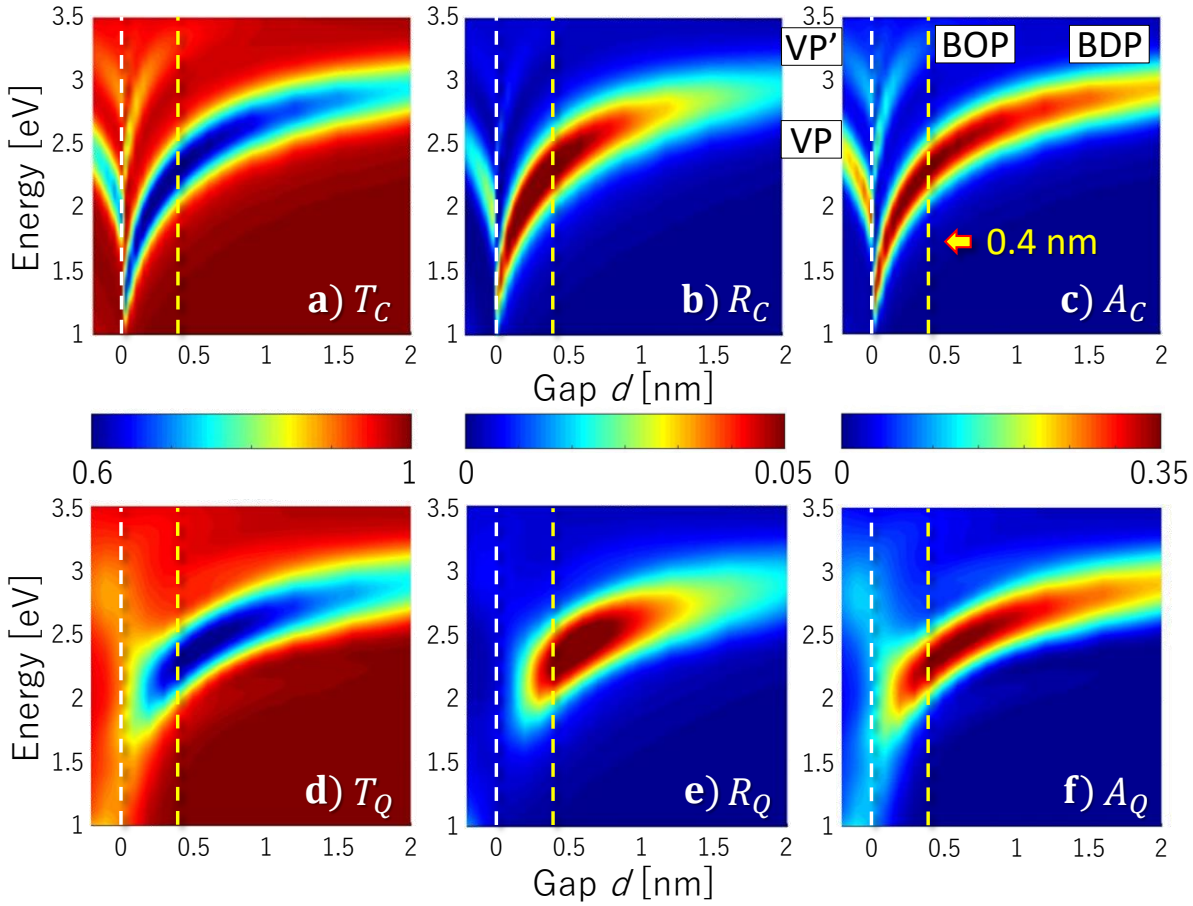

Figure 3. Spectral distributions of the transmission (T), reflection (R), and absorption (A) rates of the metasurfaces calculated by the classical theory (a–c; subscript C) and by the TDDFT (d–f; subscript Q). A common color scale applies for C and Q. All distributions are shown as functions of the gap distance d and the optical frequency. Similar to Figure 2a and 2b, the white and yellow dashed lines indicate the loci at which $d = 0$ and 0.4 nm, respectively.

We now move to our main subject of the present study. Figure 3 shows the calculated spectral distributions of the transmission (T), reflection (R), and the absorption rates (A) of the plasmonic metasurfaces for gap distances ranging from $d = -0.2$–2 nm. They are obtained by employing a 2D coarse graining approach.[37] The relevant details are described in the Supporting Information. Figure 3a–3c shows results based on the use of the classical theory, while Figure 3d–3f shows the results estimated based on the TDDFT with the use of the JM. For $d \gtrsim 0.4$ nm, the quantum and classical descriptions generate almost similar results that are characterized by a single peak derived from the BDP mode. Even though the BDP mode also appears in the isolated system, as shown in

Figure 2, we find much larger red shifts compared with the nanodimer case. This is rationalized by the fact that the constituent nanospheres in the metasurface suffer a more intense electromagnetic coupling effect compared with the dimer case owing to its periodically arrayed geometry. These features match well with those reported in the previous investigation,[16] whereby the plasmonic gap distance was explored to be as small as 0.45 nm in the measurements and simulations according to the classical theory. When $d \lesssim 0.4$ nm, the bonding octopolar plasmon (BOP) mode emerges, and is clearly visible in the classical description at a higher frequency region. Compared with the isolated system, the BQP mode does not appear in the optical response because of the full symmetry on the *xy* plane. By decreasing the distance to $d = 0$ nm or less, the void plasmon (VP) and its higher-order plasmon (VP') modes appear when the classical theory is used.

We now look into the electron transport effects at small *d* regions. As has been depicted in Figure 2c and 2d, the BDP mode disappears at $d = 0.4$ nm in the case of the nanodimer. Conversely, as observed in Figure 3d–3f, the BDP mode excited on the metasurface survives within a much smaller distance, which can be as small as $d \approx 0.2$ nm. As it has already been noted, the resonant frequency of the BDP in the metasurface is much smaller than that in the nanodimer. Thus, the changes in the optical responses caused by the classical and quantum effects are different between the nanodimer and the metasurface, reflecting their geometrical differences. These results indicate that the studied metasurface maintains a strong optical confinement and enhancement in the gap distance as small as $d \approx 0.2$ nm, which is much smaller than the critical distance $d \approx 0.4$ nm in the nanodimer. Furthermore, although the classical theory yields similar spectral distributions among *T*, *R*, and *A*, those calculated by the TDDFT yield a difference at $d \lesssim 0.2$ nm, *R* related to the BDP vanishes immediately, while *T* and *A* remain and are extensively spread in frequency, representing washed-out plasmonic features of the constituent nanoshperes in the metasurface. In particular at

d = 0 nm, R is less than 0.5%, while A is maintained at 10% in the visible frequency range. This indicates that they are suitable for an optical absorber.[43–46]

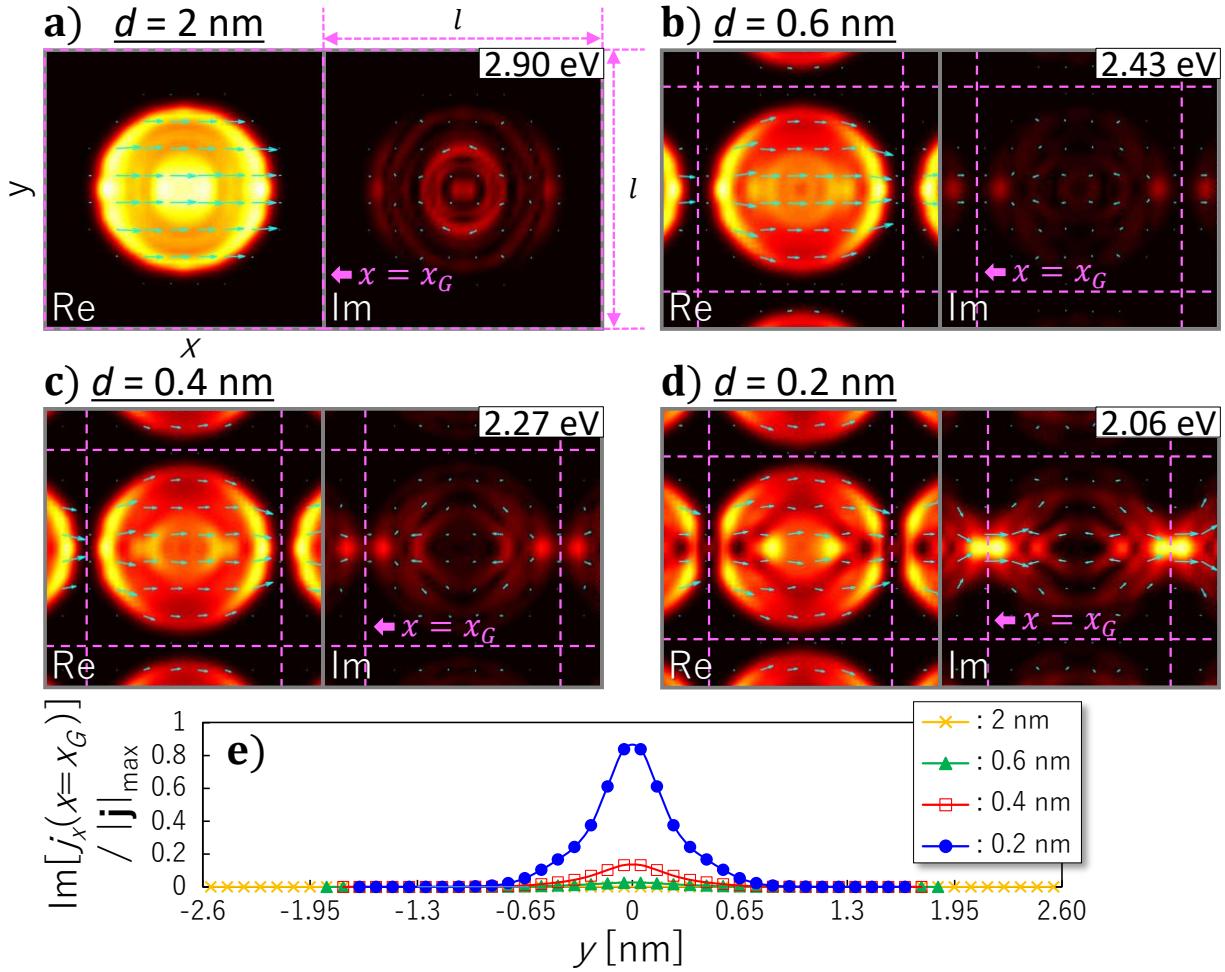

Figure 4. (a–d) Spatial distributions of electric current density on the xy plane (z = 0) at the resonant frequency of the bonding dipolar plasmon (BDP) mode, ω_{BDP} (shown in the top-right white boxes). The maximum intensity is normalized in each figure, showing $\mathbf{j}$ (x, y, z = 0, ω = ω_{BDP}) $/|\mathbf{j}|_{max}$. Real- and imaginary-parts are shown in the left and the right panels, respectively, for d = 2, 0.6, 0.4, and 0.2 nm. The light blue arrows indicate that their vector distributions with their lengths are associated with the magnitude. Dashed pink lines indicate the unit cell with a period l. The electron transport takes place through the $x = x_G$ plane. (e) The imaginary parts of the currents are displayed as a function of y at the plane $x = x_G$.

To elucidate the mechanism that produces the differences between the classical and quantum descriptions, we visualized the spatial distributions of the electric current density, $\mathbf{j}(\mathbf{r}, \omega)$, calculated by the TDDFT. For an electric field with frequency omega, $\mathbf{E}(t) = E_0\cos(\omega t)$, the electric

current density is given by $\mathbf{j}(\mathbf{r}, t) = \mathrm{Re}[\mathbf{j}(\mathbf{r}, \omega)]\cos(\omega t) - \mathrm{Im}[\mathbf{j}(\mathbf{r}, \omega)]\sin(\omega t)$. We refer to $\mathrm{Re}[\mathbf{j}(\mathbf{r}, \omega)]$ as the conductive current because it has the same phase relation to the applied electric field. Additionally, we refer to $\mathrm{Im}[\mathbf{j}(\mathbf{r}, \omega)]$ as the dielectric because it has a phase difference of $\pi/2$. Similar investigations by the classical theory are presented in the Supporting Information. Figure 4a–4d shows the electric current density in the xy plane ($z = 0$) at the resonant frequencies of the BDP mode, ω_{BDP}. The maximum value is normalized in each figure, showing $\mathbf{j}(x, y, z = 0, \omega = \omega_{BDP}) / |\mathbf{j}|_{\max}$. The real and imaginary parts of the current are shown in the left and right panels, respectively, for d = 2, 0.6, 0.4, and 0.2 nm. The light blue arrows indicate the vector distributions of the current, whereby their lengths are associated with the magnitudes. The dashed pink lines indicate the unit cell with a period l. At d = 2 nm, Re[**j**] is almost spatially uniform inside the sphere, as observed in Figure 4a. As d decreases, the currents tend to be localized at both ends of the sphere. This localization, which causes the red shift of the BDP mode as observed in Figure 3, is caused by the attractions among the positive and negative charges that appear at both ends of the neighboring nanospheres.[17, 19–22] As it has been mentioned in the Supporting Information, this behavior is also observed in the classical description. By contrast, as shown in Figure 4d, at d = 0.2 nm, the current distribution in the TDDFT shows a drastic change that is not observed in the classical theory. In Re[**j**], there appears a hole in the electric current distribution at both ends of the sphere along the $y = 0$ axis. In Im[**j**], a clear opening of the current owing to the electron transport is observed in the $x = x_G$ plane along the y axis. To elucidate the electron transport clearly, we plot the current distribution Im[**j**] against y in the $x = x_G$ plane in Figure 4e using the gap distances of Figure 4a–4d. This shows that the electron transport increases gradually as d decreases up to around 0.4 nm, and then increases abruptly toward d = 0.2nm. The $\mathbf{j}/|\mathbf{j}|_{\max}$ value at d = 0.2 nm is close to 0.9, indicating that the current is almost maximized at the gap plane x_G. This abrupt

change of the current can be rationalized by the change of the relation between the potential barrier height and the energy of the highest occupied orbital. In fact, we have found that they coincide with each other at around d = 0.3nm. Therefore, the electron transport process can be classified to the two situations: (a) At $d \gtrsim 0.3$ nm, electron transport takes place by the quantum tunneling; (b) at $d \lesssim 0.3$ nm, electron transport is dominantly caused by the over-barrier process so that a large amount of electrons can move through the gaps. The electron transport over the potential barrier rationalizes the disappearance of the BDP mode at d = 0.2nm, as shown in Figure 3d–3f, and displays the qualitative differences in the results between the quantum and the classical descriptions.

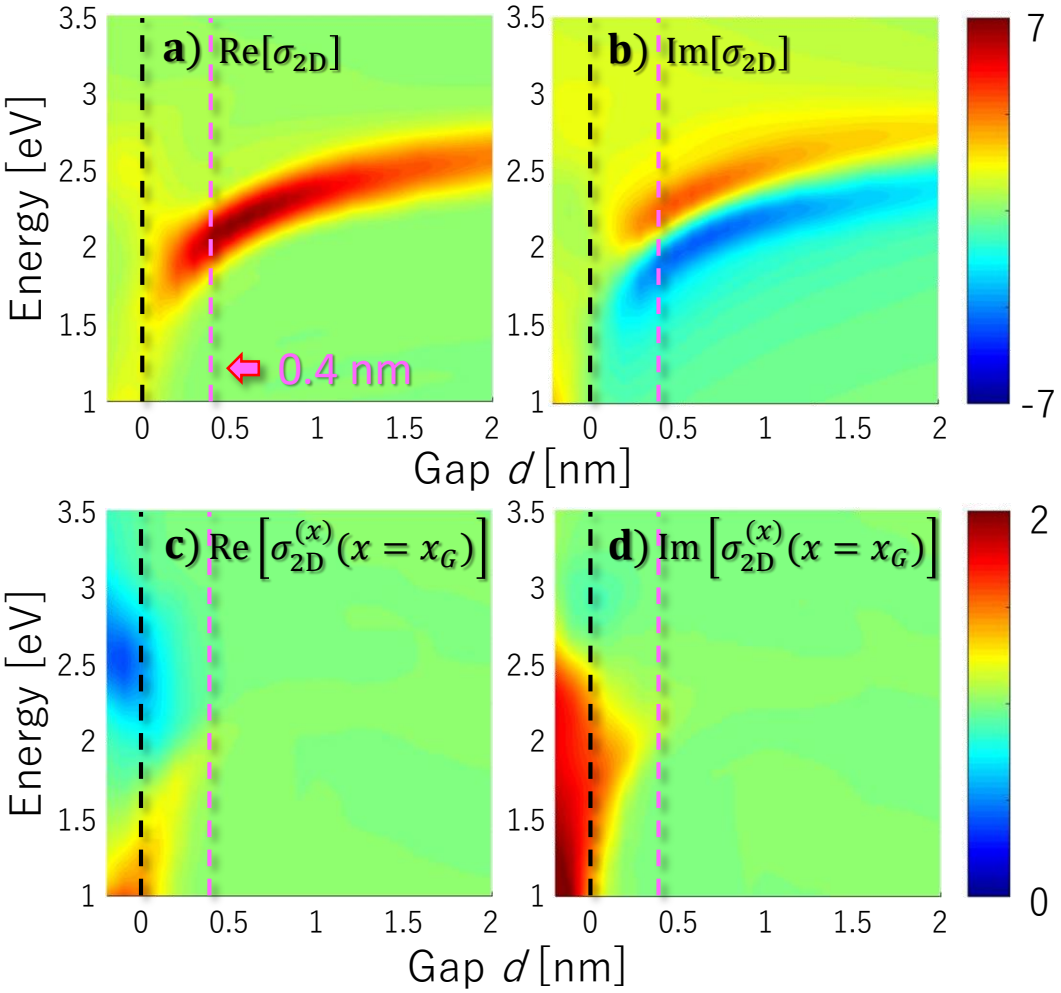

Figure 5. Spectral distributions of the two-dimensional (2D) complex conductivities of the metasurface as a function of the gap distance d (Re[σ_{2D}] is plotted in (a) and Im[σ_{2D}] in (b) in atomic units). The contributions to the 2D complex conductivity at the gap plane $x = x_G$ are shown [Re[$\sigma_{2D}^{(x)}(x = x_G)$] in (c) and Im[$\sigma_{2D}^{(x)}(x = x_G)$] in (d)]. Precise definitions are described in the Supporting Information. A common color scale applies to the real and the imaginary parts. The black and pink dashed lines indicate the loci at which d = 0 nm and 0.4 nm, respectively.

To clarify the effects of electron transport within the entire spectral region, we show the spectral distributions of the 2D complex conductivity of the metasurface, with Re[σ_{2D}] and Im[σ_{2D}] in atomic units in Figure 5a and 5b, respectively. The optical quantities T, R, and A, in Figure 3d–3f are obtained from the 2D conductivity. As explained in the Supporting Information, it is possible to express the 2D conductivity as an integration over x, $\sigma_{2D}(\omega) = (\frac{1}{l})\int dx \sigma_{2D}^{(x)}(x, \omega)$. Figure 5c

and 5d show a contribution at the gap plane, $x = x_G$, to the conductivity, $\mathrm{Re}[\sigma_{2D}^{(x)}(x = x_G)]$ and $\mathrm{Im}[\sigma_{2D}^{(x)}(x = x_G)]$. In the region $0 < d < 0.2$ nm, a negative contribution (blue-colored region) appears in $\mathrm{Re}[\sigma_{2D}^{(x)}(x = x_G)]$. This is caused by the current density of the VP mode whose direction is reversed around the gap plane $x = x_G$. In $\mathrm{Im}[\sigma_{2D}^{(x)}(x = x_G)]$ in $d < 0.2$ nm, a positive contribution appears in the broad frequency region. As observed from Figure 5c and 5d, which displays $\mathrm{Re}[\sigma_{2D}^{(x)}(x = x_G)]$ and $\mathrm{Im}[\sigma_{2D}^{(x)}(x = x_G)]$, the electron transport at the gap plane $x = x_G$ contributes substantially to the 2D conductivity. Based on this result, we conclude that the onset of electron transport is at approximately $d \approx 0.2$ nm.

The execution of this study was based on various approximations, which are outlined below in conjunction with the limitations of this study. Although the JM is known to provide a reasonable description for plasmonic features of metallic nanoparticles, descriptions of the tunneling effect between nanoparticles may not be realistic enough because the tunneling is sensitive to a precise structure at the interfaces at the atomic scale, as has been shown in recent studies.[21] Electron tunneling was studied[21] in a metallic nanodimer consisting of realistic Na clusters. This study revealed that the JM could not account for the lightning rod effect that is caused by the electron concentration at the edges of the clusters. First-principles calculations that incorporate precise ionic structures could account for these effects in our targeting metasurface. However, in practice, this is a rather difficult task because the shapes of the fabricated nanoparticles arrayed on the metasurface are quite random.[15–16] Accordingly, we could not apply the periodic boundary condition that was used in the present work.

Although we have considered very small nanoparticles whose diameters are 3.1 nm, insights into the electron transport should have robustness for larger systems because previous studies that

dealt with nanodimers showed substantial agreements despite the spatial scale differences between theory and measurements.[21] To explore the electron tunneling effects, the quantum corrected model (QCM)[19] was developed and successfully applied to isolated systems, such as nanodimers. This model is based on the classical theory with some modifications that take into account the electron tunneling effects. While the TDDFT has been used in this study, the QCM is also a prospective candidate for the exploration of quantum plasmonic metasurfaces with subnanometer gaps. Furthermore, given that the QCM requires a moderate computational cost compared with the expensive TDDFT, it will be useful for investigating larger systems. We consider that the application of the QCM to the metallic metasurface and the comparison with the TDDFT results is an important topic for a future study.

In conclusion, this study has presented a theoretical investigation into quantum plasmonic metasurfaces with subnanometer gaps. The optical responses of a metasurface composed of two-dimensionally arrayed metallic nanospheres have been examined based on the use of the TDDFT with the JM. We have shown the transmission, reflection, and absorption rates of the metasurface as a function of the gap distance. It has been shown that substantial differences exist between the classical and the quantum theories when the gap distances become less than approximately 0.2 nm owing to the electron transport. This threshold distance is almost half of the typical threshold distance known for isolated systems, such as metallic nanodimers. It has also been shown that the quantum effects make the plasmon features washed out and produce broad spectral structures in the optical responses. In particular, the reflection shows rapid attenuation as the gap distance decreases, while the absorption response is maintained over a broader spectral range. The knowledge obtained in this study is expected to be beneficial in view of the growing interests in metasurfaces with gap plasmonics, and will provide relevant guidelines for their design.

ASSOCIATED CONTENT

Supporting Information

Detailed theoretical descriptions of 2D coarse graining approach, the TDDFT, and classical theory with plasmonic responses are given. This material is submitted as a separate file.

AUTHOR INFORMATION

Corresponding Author

*E-mail: take@ccs.tsukuba.ac.jp

Author Contributions

Funding Sources

This research was supported by the JST–CREST under Grant No. JP–MJCR16N5, and by the JSPS KAKENHI under Grant No. 15H03674.

ACKNOWLEDGMENT

Theoretical computations were performed in part with the use of the computational resources of Oakforest–PACS provided by the Multidisciplinary Cooperative Research Program in Center for Computational Sciences, University of Tsukuba, and the Research Center for Computational Science, Okazaki, Japan.

REFERENCES

(1) Meinzer, N.; Barnes, W. L.; Hooper, I. R. Plasmonic meta-atoms and metasurfaces. *Nat. Photonics* **2014**, *8*, 889.

(2) Choudhury, S. M.; Wang, D.; Chaudhuri, K.; DeVault, C.; Kildishev, A. V.; Boltasseva, A.; Shalaev, V. M. Material platforms for optical metasurfaces. *Nanophotonics* **2018**, *7*, 959.

(3) Aieta, F.; Genevet, P.; Kats, M. A.; Yu, N.; Blanchard, R.; Gaburro, Z.; Capasso F. Aberration-Free Ultrathin Flat Lenses and Axicons at Telecom Wavelengths Based on Plasmonic Metasurfaces. *Nano Lett.* **2012**, *12*, 4392.

(4) Khorasaninejad, M.; Chen, W. T.; Devlin, R. C.; Oh, J.; Zhu, A. Y.; Capasso, F. Metalenses at visible wavelengths: Diffraction-limited focusing and subwavelength resolution imaging. *Science* **2016**, *352*, 6290.

(5) Chen, W. T.; Yang, K. Y.; Wang, C. M.; Huang, Y. W.; Sun, G.; Chiang, I. D.; Liao, C. Y.; Hsu, W. L.; Lin, H. T.; Sun, S.; Zhou, L.; Liu, A. Q.; Tsai, D. P. High-Efficiency Broadband Meta-Hologram with Polarization-Controlled Dual Images. *Nano Lett.* **2014**, *14*, 225.

(6) Zheng, G.; Mühlenbernd, H.; Kenney, M.; Li, G.; Zentgraf, T.; Zhang, S. Metasurface holograms reaching 80% efficiency. *Nat. Nanotech.* **2015**, *10*, 308.

(7) Huang, Y. W.; Chen, W. T.; Tsai, W. Y.; Wu, P. C.; Wang, C. M.; Sun, G.; Tsai, D. P. Aluminum Plasmonic Multicolor Meta-Hologram. *Nano Lett.* **2015**, *15*, 3122.

(8) Li, X.; Chen, L.; Li, Y.; Zhang, X.; Pu, M.; Zhao, Z.; Ma, X.; Wang, Y.; Hong, M.; Luo, X. Multicolor 3D meta-holography by broadband plasmonic modulation. *Sci. Adv.* **2016**, *2*, e1601102.

(9) Yu, N.; Aieta, F.; Genevet, P.; Kats, M. A.; Gaburro, Z.; Capasso, F. A Broadband, Background-Free Quarter-Wave Plate Based on Plasmonic Metasurfaces. *Nano Lett.* **2012**, *12*, 6328.

(10) Ding, F.; Wang, Z.; He, S.; Shalaev, V. M.; Kildishev, A. V. Broadband High-Efficiency Half-Wave Plate: A Supercell-Based Plasmonic Metasurface Approach. *ACS Nano* **2015**, *9*, 4111.

(11) Ishii, S.; Kildishev, A. V.; Shalaev, V. M.; Chen, K. P.; Drachev, V. P. Metal nanoslit lenses with polarization-selective design. *Opt. Lett.* **2011**, *36*, 451.

(12) Yang, Y.; Wang, W.; Moitra, P.; Kravchenko, I. I.; Briggs, D. P.; Valentine, J. Dielectric Meta-Reflectarray for Broadband Linear Polarization Conversion and Optical Vortex Generation. *Nano Lett.* **2014**, *14*, 1394.

(13) Li, Z.; Palacios, E.; Butun, S.; Aydin, K. Visible-Frequency Metasurfaces for Broadband Anomalous Reflection and High-Efficiency Spectrum Splitting. *Nano Lett.* **2015**, *15*, 1615.

(14) Ni, X.; Wong, Z. J.; Mrejen, M.; Wang, Y.; Zhang, X. An ultrathin invisibility skin cloak for visible light. *Science* **2015**, *349*, 1310.

(15) Fontana, J.; Maldonado, M.; Charipar, N.; Trammell, S. A.; Nita, R.; Naciri, J.; Pique, A.; Ratna, B.; Gomes, A. S. L. Linear and nonlinear optical characterization of self-assembled, large-area gold nanosphere metasurfaces with sub-nanometer gaps. *Opt. Express.* **2016**, *24*, 27360.

(16) Doyle, D.; Charipar, N.; Argyropoulos, C.; Trammell, S. A.; Nita, R.; Naciri, J.; Piqué, A.; Herzog, J. B.; Fontana, J. Tunable Subnanometer Gap Plasmonic Metasurfaces. *ACS Photo.* **2018**, 5, 1012.

(17) Zuloaga, J.; Prodan, E.; Nordlander, P. Quantum Description of the Plasmon Resonances of a Nanoparticle Dimer. *Nano Lett.* **2009**, *9*, 887.

(18) Marinica, D. C.; Kazansky, A. K.; Nordlander, P.; Aizpurua, J.; Borisov, A. G. Quantum Plasmonics: Nonlinear Effects in the Field Enhancement of a Plasmonic Nanoparticle Dimer. *Nano Lett.* **2012**, *12*, 1333.

(19) Esteban, R.; Borisov, A. G.; Nordlander, P.; Aizpurua, J. Bridging quantum and classical plasmonics with a quantum-corrected model. *Nat. Commun.* **2012**, *3*, 825.

(20) Scholl, J. A.; García-Etxarri, A.; Koh, A. L.; Dionne, J. A. Observation of Quantum Tunneling between Two Plasmonic Nanoparticles. *Nano Lett.* **2012**, *12*, 1333.

(21) Barbry, M.; Koval, P.; Marchesin, F.; Esteban, R.; Borisov, A. G.; Aizpurua, J.; Sánchez-Portal, D. Atomistic Near-Field Nanoplasmonics: Reaching Atomic-Scale Resolution in Nanooptics. *Nano Lett.* **2015**, *15*, 3410.

(22) Varas, A.; García-González, P.; Feist, J.; García-Vidal, F. J.; Rubio, A. Quantum plasmonics: from jellium models to ab initio calculations. *Nanophotonics* **2016**, *5*, 409.

(23) Aguirregabiria, G.; Marinica, D. C.; Esteban, R.; Kazansky, A. K.; Aizpurua, J.; Borisov, A. G. Role of electron tunneling in the nonlinear response of plasmonic nanogaps. *Phys. Rev. B* **2018**, *97*, 115430.

(24) Mao, L.; Li, Z.; Wu, B.; Xu, H. Effects of quantum tunneling in metal nanogap on surface-enhanced Raman scattering. *Appl. Phys. Lett* **2009**, *94*, 243102.

(25) Savage, K. J.; Hawkeye, M. M.; Esteban, R.; Borisov, A. G.; Aizpurua, J.; Baumberg, J. J. Revealing the quantum regime in tunnelling plasmonics. *Nature* **2012**, *491*, 574.

(26) Scholl, J. A.; Garcia-Etxarri, A.; Aguirregabiria, G.; Esteban, R.; Narayan, T. C.; Koh, A. L.; Aizpurua, J.; Dionne, J. A. Evolution of Plasmonic Metamolecule Modes in the Quantum Tunneling Regime. *ACS Nano* **2016**, *10*, 1346.

(27) Kneipp, K.; Wang, Y.; Kneipp, H.; Perelman, L. T.; Itzkan, I.; Dasari, R. R.; Feld, M. S. Single Molecule Detection Using Surface-Enhanced Raman Scattering (SERS). *Phys. Rev. Lett.* **1997**, *78*, 1167.

(28) Nie, S.; Emory, S. R. Probing Single Molecules and Single Nanoparticles by Surface-Enhanced Raman Scattering. *Science* **1997**, *275*, 1102.

(29) Xu, H.; Bjerneld, E. J.; Käll, M.; Börjesson, L. Spectroscopy of Single Hemoglobin Molecules by Surface Enhanced Raman Scattering. *Phys. Rev. Lett.* **1999**, *83*, 4357.

(30) Lim, D. K.; Jeon, K. S.; Hwang, J. H.; Kim, H.; Kwon, S.; Suh, Y. D.; Nam, J. M. Highly uniform and reproducible surface-enhanced Raman scattering from DNA-tailorable nanoparticles with 1-nm interior gap. *Nat. Nanotech.* **2011**, *6*, 452.

(31) Anker, J. N.; Hall, W. P.; Lyandres, O.; Shah, N. C.; Zhao, J.; Van Duyne, R. P. Biosensing with plasmonic nanosensors. *Nat. Mat.* **2008**, *7*, 442.

(32) Boltasseva, A.; Atwater, H. A. Low-Loss Plasmonic Metamaterials. *Science* **2011**, *331*, 290.

(33) Yu, N.; Genevet, P.; Kats, M. A.; Aieta, F.; Tetienne, J. P.; Capasso, F.; Gaburro, Z. Light Propagation with Phase Discontinuities: Generalized Laws of Reflection and Refraction. *Science* **2011**, *334*, 333.

(34) Polman, A.; Atwater, H. A. Photonic design principles for ultrahigh-efficiency photovoltaics. *Nat. Mat.* **2012**, *11*, 174.

(35) Runge, E.; Gross, E. K. U. Density-Functional Theory for Time-Dependent Systems. *Phys. Rev. Lett.* **1984**, *52*, 997.

(36) Ullrich, C. A. *Time-Dependent Density-Functional Theory Concepts and Applications*; Oxford University Press, 2012.

(37) Yamada, S.; Noda, M.; Nobusada, K.; Yabana, K. Time-dependent density functional theory for interaction of ultrashort light pulse with thin materials. *Phys. Rev. B* **2018**, *98*, 245147.

(38) Brack, M. The physics of simple metal clusters: self-consistent jellium model and semiclassical approaches. *Rev. Mod. Phys.* **1993**, *65*, 677.

(39) Yabana, K.; Bertsch, G. F. Time-dependent local-density approximation in real time. *Phys. Rev. B* **1996**, *54*, 4484.

(40) Bertsch, G. F.; Iwata, J. I.; Rubio, A.; Yabana, K. Real-space, real-time method for the dielectric function. *Phys. Rev. B* **2000**, 62, 7998.

(41) Perdew, J. P.; Zunger, A. Self-interaction correction to density-functional approximations for many-electron systems. *Phys. Rev. B* **1981**, *23*, 5048.

(42) Noda, M.; Sato, S. A.; Hirokawa, Y.; Uemoto, M.; Takeuchi, T.; Yamada, S.; Yamada, A.; Shinohara, Y.; Yamaguchi, M.; Iida, K.; Floss, I.; Otobe, T.; Lee, K. M.; Ishimura, K.; Boku, T.; Bertsch, G. F.; Nobusada, K.; Yabana, K. SALMON: Scalable Ab-initio Light–Matter simulator for Optics and Nanoscience. *Comput. Phys. Commun.* **2019**, *235*, 356.

(43) Jiang, Z. H.; Yun, S.; Toor, F.; Werner, D. H.; Mayer, T. S. Conformal Dual-Band Near-Perfectly Absorbing Mid-Infrared Metamaterial Coating. *ACS Nano* **2011**, *5*, 4641.

(44) Aydin, K.; Ferry, V. E.; Briggs, R. M.; Atwater, H. A. Broadband polarization-independent resonant light absorption using ultrathin plasmonic super absorbers. *Nat. Commun.* **2011**, *2*, 517.

(45) Argyropoulos, C.; Le, K. Q.; Mattiucci, N.; D'Aguanno, G.; Alù, A. Broadband absorbers and selective emitters based on plasmonic Brewster metasurfaces. *Phys. Rev. B* **2013**, *87*, 205112.

(46) Ding, F.; Dai, J.; Chen, Y.; Zhu, J.; Jin, Y.; Bozhevolnyi, S. I. Broadband near-infrared metamaterial absorbers utilizing highly lossy metals. *Sci. Rep.* **2016**, 6, 39445.